Article

Straightened Segmentation in 4D Cardiac CT: A Practical Method for Multiparametric Characterization of the Landing Zone for Transcatheter Pulmonary Valve Replacement

Xiaolin Sun [1,2,3,†], Yimeng Hao [1,2,†], Marvin Steitz [1,2], Alexander Breitenstein-Attach [1,2], Jonathan Frederik Sebastian Kiekenap [1], Jasper Emeis [1], Mahamuda Badhon Khan [1], Felix Berger [1,2] and Boris Schmitt [1,2,3,4,5*]

[1] Department of Pediatric Cardiology and Congenital Heart Disease, Charité University Medicine Berlin, Augustenburger Platz 1, 13353 Berlin, Germany
[2] Department of Pediatric Cardiology and Congenital Heart Disease, Deutsches Herzzentrum Berlin, Augustenburger Platz 1, 13353 Berlin, Germany
[3] DZHK (German Centre for Cardiovascular Research), Potsdamer Straße 58, 10785 Berlin, Germany
[4] BIH (Berlin Institute of Health), Anna-Louisa-Karsch-Straße 2, 10178 Berlin, Germany
[5] BCRT (BIH Center of Regenerative Therapies), Föhrer Straße 15, 13353 Berlin, Germany
* Correspondence: schmitt@dhzb.de; Tel.: +49-(0)30-4593-2875
† These authors have contributed equally to this work and share first authorship.

Featured Application: Four-dimensional cardiac straightened segmentation can be useful for the periprocedural evaluation of TPVR.

Abstract: Cardiac computed tomography angiography (C-CTA) is crucial in assessing the right ventricular outflow tract (RVOT) prior to a transcatheter pulmonary valve replacement (TPVR), as an incorrect evaluation can make the procedure more challenging and can lead to device-related complications. This study aimed to evaluate the feasibility and accuracy of 4D straightened segmentation for a landing zone analysis over anatomical segmentation. Seven pre-operative CTAs and seven post-operative CTAs were used to measure the cross-sectional area, circumference, and diameters at five selected planes as the landing zone for TPVR and compared these to the 4D straightened model with the anatomical model. Furthermore, the right ventricular volume, stent volume, and 4D ellipticity index were calculated from the 4D straightened model. The 4D straightened segmentation had comparable accuracy and efficacy for the measurements at the landing zone. The cross-sectional area and the circumference varied greatly at the RVOT and the basal plane of the pulmonary valve compared with the other three planes of the 4D straightened models from the pre-operative CTAs; however, only the values at the RVOT were found to vary greatly from the post-operative CTAs. The 4D straightened model can provide accurate measurements and is thus a useful method for the periprocedural evaluation of TPVR.

Keywords: four-dimensional computed tomography; transcatheter pulmonary valve replacement; cardiac catheterization; 4D dynamic segmentation; landing zone

1. Introduction

Transcatheter pulmonary valve replacement (TPVR) is a well-established alternative therapeutic approach for patients with right ventricular outflow tract (RVOT) dysfunction, the majority of whom are young and suffer from congenital heart defects or have had multiple previous cardiac surgeries [1,2]. Recent studies show that, in terms of survival and freedom from reintervention or surgery, the outcomes of TPVR are comparable with those of surgical conduit/valve replacement to manage RVOT dysfunction across a

wide age range [3,4]. Similar to transcatheter aortic valve replacement (TAVR), cardiac computed tomography angiography (C-CTA) plays a crucial role in the characterization of the morphology, distensibility, and compliance of the RVOT prior to TPVR, since inaccurate sizing can complicate the procedure and cause device-related complications, such as embolization and paravalvular leak (PVL) [5,6].

Technological developments in three-dimensional (3D) and four-dimensional (4D) C CTA have opened the door to a novel method for the personalized planning of transcatheter heart valve implantation for patients with structural heart valve diseases [7–9]. Cross-sectional imaging with 3D and 4D C-CTA is critical to determine patients' suitability for TPVR; knowledge of RVOT anatomy, the proximity of the left coronary artery to the native pulmonary root, and the distensibility of the RVOT are indispensable for TPVR [10,11]. In addition to this, 3D and 4D C-CTA can support the identification of candidate percutaneous access routes, including the transfemoral, transjugular, and subclavian routes, and answer key anatomical questions. Furthermore, the landing zone—the ideal implantation site for TPVR—can protect the stented pulmonary valve (PV) from PVL, migration, and coronary compression. To create an accurate 4D segmentation of the landing zone anatomy at the RVOT, CT datasets should undergo segmentation where the personalized CT data are assigned to a region of interest to generate the 4D structures in synchronization with the heart rate. A previous study showed that the RVOT's morphology and size can vary significantly throughout the entire cardiac cycle, and so perimeter- and cross-sectional area-based measurements have proven more reliable than PV annulus diameters alone [12]. Additionally, the necessity of 4D C-CTA is emphasized by Gillespie and colleagues, who encourage taking measurements for the landing zone both during end-systole and end-diastole phases [13].

However, in current traditional clinical and preclinical settings, the resulting 4D CT data are frequently transformed into 3D data for manual quantification and visual evaluation, which can only show static information. Furthermore, anatomical 4D segmentations are unable to fully depict the characteristics of the RVOT adjacent to the aortic root during the course of the cardiac cycle, even with 4D information. Yet, the 4D dynamic volumes of the right ventricle, implanted stent, and landing zone, which are crucial for the quantitative interpretation of TPVR, are only partially illustrated by the available data. In addition to the 4D anatomical segmentation, the angle between the RVOT and the main pulmonary artery can cause the measuring lines to not fully align with the landing zone planes (e.g., the annular plane or sinotubular junction plane), which can result in incorrect landing zone measurements. The 2D properties of the STJ plane, the sinus plane and the pulmonary valve annular plane, are defined by three points at each level—the three commissures, the petaline peak of the sinuses, and the nadir of the pulmonary valve—instead of 3D properties, which could lead to inaccurate landing zone measurements. Multi-planar measurements are often employed in clinical practice to assess the RVOT before TPVR, but due to their 3D properties, planes may be positioned incorrectly in anatomical segmentations.

In this study, we exploited a practical approach to performing multiparametric analyses of pre- and post-interventional C-CTA for TPVR in a sheep model by straightening the 4D anatomical segmentations into a 4D straightened segmentation. Our primary objective was to evaluate the feasibility and accuracy of 4D straightened segmentation in comparison to traditional anatomical segmentation, identify its benefits, and explore its potential as a complementary planning tool in TPVR.

2. Materials and Methods

This study included seven adult sheep (Ovis aries), all of which received humane care in compliance with the guidelines of the European and German Societies of Laboratory Animal Science (FELASA, GV-SOLAS). The legal and ethical committee of the Regional Office for Health and Social Affairs in Berlin (LaGeSo) approved the GrOwnValve preclinical trial aiming to conduct transcatheter pulmonary valve replacement from

autologous pericardium with a self-expandable stent in a sheep model (IC14-G 0062/18). The TPVRs were performed at Charité University Hospital of Berlin, Campus Virchow-Klinikum, Research Institute for Experimental Medicine (FEM), while all 4D cardiac CTs were performed at the German Heart Center Berlin.

2.1. Scan Protocol and 4D Cardiac CT Processing

All cardiac CTAs were performed on a Siemens 64-slice dual-source multidetector CT scanner with ECG gating (SOMATOM Definition Flash, Siemens AG, Munchen, Germany). The sheep were scanned in the prone position with standard acquisition technical parameters: a gantry rotation time of 0.33 s, 100–320 mAs per rotation, a 120 kV tube voltage, matrix 256 with a 16-bit depth, a deviation effective X-ray dose of 15.5 ± 11.6 mSv, and a slice thickness of 0.75 mm. CT contrast enhancement was achieved by administering 2–2.5 mL/kg of an iodinated contrast agent at a rate of 5 mL/s. To achieve the ideal synchronization, a bolus tracking method was used for contrast bolus timing in the region of interest on the main pulmonary artery. The 4D cardiac CTA scanning protocol produced 10 continuous frames for the cardiac cycle, from 10% to 100%, with 10% of the RR interval covering the entire cardiac cycle.

2.2. Four-Dimensional Cardiac CT Analysis in 3D Slicer

2.2.1. Segmentations

The CT data of the seven sheep were processed offline using the open-source software 3D Slicer (https://www.slicer.org/ (accessed on 1 March 2022). The 4D anatomical right heart (from the superior vena cava to the end of the main pulmonary artery, without the inferior vena cava) blood pool was segmented using a certain threshold automatically and manually based on each C-CTA by two experienced doctors and optimized manually by a senior expert. The inferior vena cava was not included in this anatomical segmentation due to its low contrast (the contrast agent was administered via the cephalic vein) and the establishment of the subsequent straightened segmentation.

After creating the anatomical segmentation for each 10% of cardiac cycle, the straightened 4D right heart segmentations were created as follows. Two markup points were placed on the top plane of the superior vena cava and the end plane of the main pulmonary artery to construct a centerline for each anatomical segmentation, and then a centerline curve was generated by adding a new markup curve to the segmentation. An output straightened volume was created by executing the "Curved Planar Reformat" operation. This straightened volume was then used to construct a straightened segmentation both automatically and manually. The segmentation for each 10% of the cardiac cycle was obtained using the same methods. The ten 3D straightened segmentations were sequentially concatenated to create a 4D straightened right heart segmentation.

The straightened 4D right heart models were created by adding centerlines and curved planar reformatting to the corresponding anatomical model. Similar steps were used for all segmentations of both the pre-operative C-CTA (pre-CT) and post-operative C-CTA (post-CT). Comprehensive steps for the 4D cardiac CTA analysis were described previously [14].

2.2.2. Multiparametric Measurements of the Landing Zone

Dynamic landing zone measurements, which included cross-sectional area, circumference, maximum diameter, and minimum diameter in the pre-CTs, were taken in five planes at the landing zone: plane 1—RVOT (10 mm below plane 2), plane 2—BPV plane (three hinge points at the nadir of each of the attachments of the PV), plane 3—sinus plane, plane 4—sinotubular junction (STJ) plane, and plane 5—PA plane (10 mm above plane 4). The five planes in the post-CTs were defined as follows: plane 1—RVOT (10 mm below plane 2), plane 2—bottom plane of the stent (BPS) plane, plane 3—middle plane of the stent (MPS) plane, plane 4—top plane of the stent (TPS) plane, and plane 5—PA plane (10

mm above plane 4) (Figure 1). The RV volume was obtained by cutting the right heart segmentations at the tricuspid valve level and at the level of plane 4 both in the anatomical and the straightened segments. The right ventricular ejection fraction (RVEF) can be calculated using the minimum and maximum RV volume. The volume of the landing zone in the pre- (PV volume) and post-CTs (stent volume, SV) was obtained by cutting the right heart segments from plane 1 to plane 5 both in the anatomical and the straightened segments. The rendered stent volume in the post-CTs was created by masking the right heart volume between plane 2 and 4 for the entire cardiac cycle. The ratio between the minimum and maximum diameter in each section was calculated to determine the grade of the elliptical shape (ellipticity index). The correlation between the anatomical model and straightened model was assessed using the Pearson correlation coefficient. We calculated the *r* value for the Pearson correlation coefficient using Formula (1),then obtained the *t* value using Formula (2). In the case where the degrees of freedom (d.f.) for *r* is *n* − 2, the *p* value can be obtained using the critical values of *t* for Pearson's *r*.

$$r = \frac{n \sum x_i y_i - \sum x_i \sum y_i}{\sqrt{n \sum x_i^2 - (\sum x_i)^2} \sqrt{n \sum y_i^2 - (\sum y_i)^2}} \tag{1}$$

$$t = \frac{r}{\sqrt{\frac{1 - r^2}{n - 2}}} \tag{2}$$

Bland–Altman analysis was conducted to further confirm the agreement between the two models.
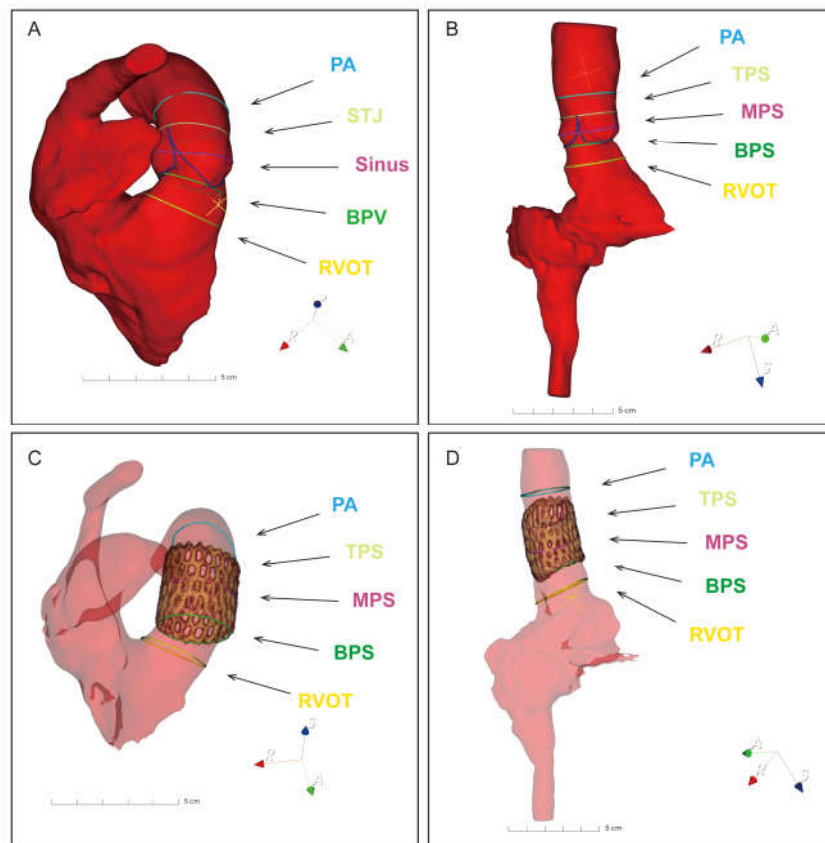

Figure 1. Five selected planes from different segmentations. (**A**) anatomical model from pre-operative CT, (**B**) straightened model from pre-operative CT, (**C**) anatomical model from post-CT, (**D**) straightened model from post-CT. PA pulmonary artery, STJ sinotubular junction, BPV basal plane

of pulmonary valve, RVOT right ventricular outflow tract, TPS top plane of the stent, MPS middle plane of the stent, BPS bottom plane of the stent.

2.3. TPVR Protocol

The sheep were tranquilized with an intramuscular injection of 0.4 mg/kg of midazolam, 0.4 mg/kg of butorphanol, and 0.011 mg/kg of glycopyrronium bromide. After administering intravenous anesthesia by injecting 1–2.5 mg/kg of propofol and 0.01 mg/kg of fentanyl, the sheep were intubated, and a gastric tube was placed into the stomach for gas and fluid evacuation during the preparation for CT and TPVR.

The sheep were ventilated under general anesthesia, which was maintained by isoflurane (1%) in oxygen (flow = 1 L/min, FiO2 = 75%), combined with a continuous rate infusion of fentanyl (5–15 mcg/kg/h) and midazolam (0.2–0.5 mg/kg/h) during the left mini-thoracotomy to harvest the autologous pericardium and perform the transjugular implantation of the autologous heart valve. GrOwnValve sizing was achieved according to the 4D measurements of the landing zone in the pre-CTs (Figure 1A). The autologous pericardium was harvested to manufacture a new PV by trimming and sewing it onto a Nitinol stent. The stented autologous PVs were loaded into the head of a self-designed delivery system and advanced via the left jugular vein under guidewire and fluoroscopy guidance. After confirmation of the deployment position in the right heart angiography, the GrOwnValve was deployed at the native PV position. The protocol for the GrOwnValve transjugular vein implantation was illustrated in detail previously [15].

2.4. Statistical Analysis

Statistics were analyzed using the GraphPad Prism 9 software (Graphpad Software, Biomatters, Ltd., NZ, and GSL Biotech, San Diego, CA, USA). Normal distribution was assessed with a Kolmogorov–Smirnov test. Continuous variables are presented as mean ± standard deviation (SD) for normal distribution or as median with interquartile ranges (IQRs) for non-normal distribution. The Pearson correlation coefficient was used to quantify the correlation between each plane of the anatomical model and the straightened model during the ten cardiac phases for each of the seven sheep. The agreement and bias between the two models were assessed with Bland–Altman analysis. A p value of < 0.05 was considered statistically significant. All the test results are two-tailed.

3. Results

3.1. Four-Dimensional Cardiac CT Segmentation

Fourteen C-CTA datasets (a pre-CT and a post-CT from each of the seven sheep) were included in the study. Each CT was divided into ten cardiac phases. Furthermore, each CT was reconstructed into an anatomical model and a straightened model. In total, 28 anatomical models and straightened models were successfully segmented and reconstructed from the 14 CTs. The cross-sectional area, circumference, maximum diameter, and minimum diameter of the five planes were measured for each model. This resulted in a total of 350 paired datasets in each measurement that were acquired at the 10 different cardiac cycles between the anatomical model and the straightened model. In addition, the parameters for a single plane were compared as well.

3.2. Correlations between Anatomical Model and Straightened Model

In all pre-CT comparisons, there was a strong linear correlation between the anatomical model and the straightened model for the cross-sectional area and the circumference measurements at all five planes, with a Pearson correlation coefficient of 0.95 ($p < 0.0001$) for the cross-sectional area and 0.94 ($p < 0.0001$) for the circumference. The Bland–Altman analysis further confirmed a strong agreement between the two models (Figure 2).
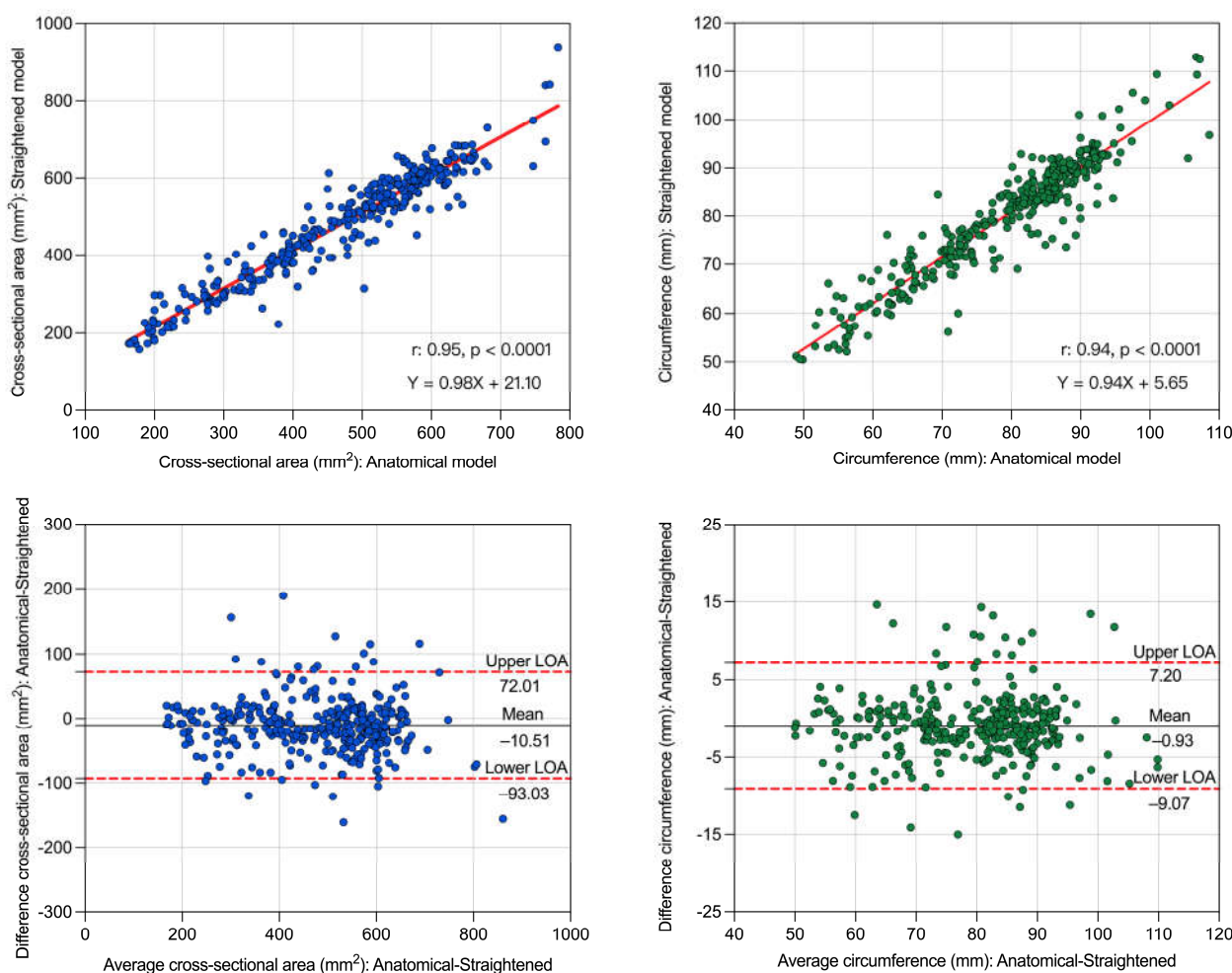
Figure 2. Pearson correlation scatterplot and Bland–Altman plot of cross-sectional area and circumference for the agreement between the anatomical model and straightened model from pre-CT. LOA—limit of agreement.

Similarly, the two pre-CT models for the minimum and maximum diameter were highly correlated, with a Pearson correlation coefficient of 0.96 ($p < 0.0001$) for the minimum diameter and 0.91 ($p < 0.0001$) for the maximum diameter. The limits of agreement between the anatomical model and the straightened model were in a good range for both the minimum diameter and maximum diameter (Figure 3).
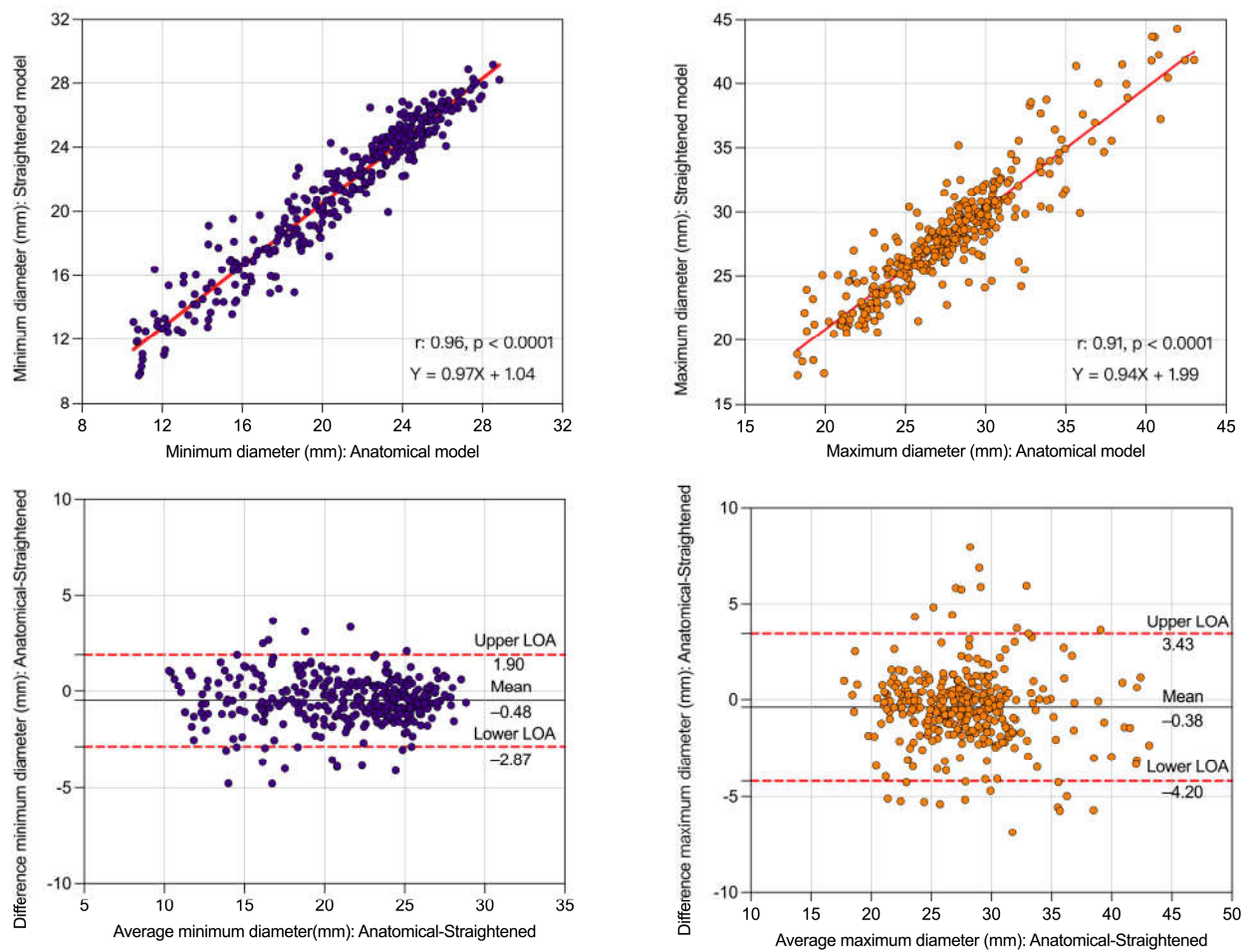
Figure 3. Pearson correlation scatterplot and Bland–Altman plot of minimum diameter and maximum diameter for the agreement between anatomical model and straightened model from pre-CT. LOA—limit of agreement.

There was also a statistically significant linear correlation between the cross-sectional area (*r*: 0.97, *p* < 0.0001) and the circumference (*r*: 0.97, *p* < 0.0001) of the two models for the post-CTs (Figure 4). The scatter plot of the Bland–Altman analysis also demonstrates good agreement for every paired dataset.
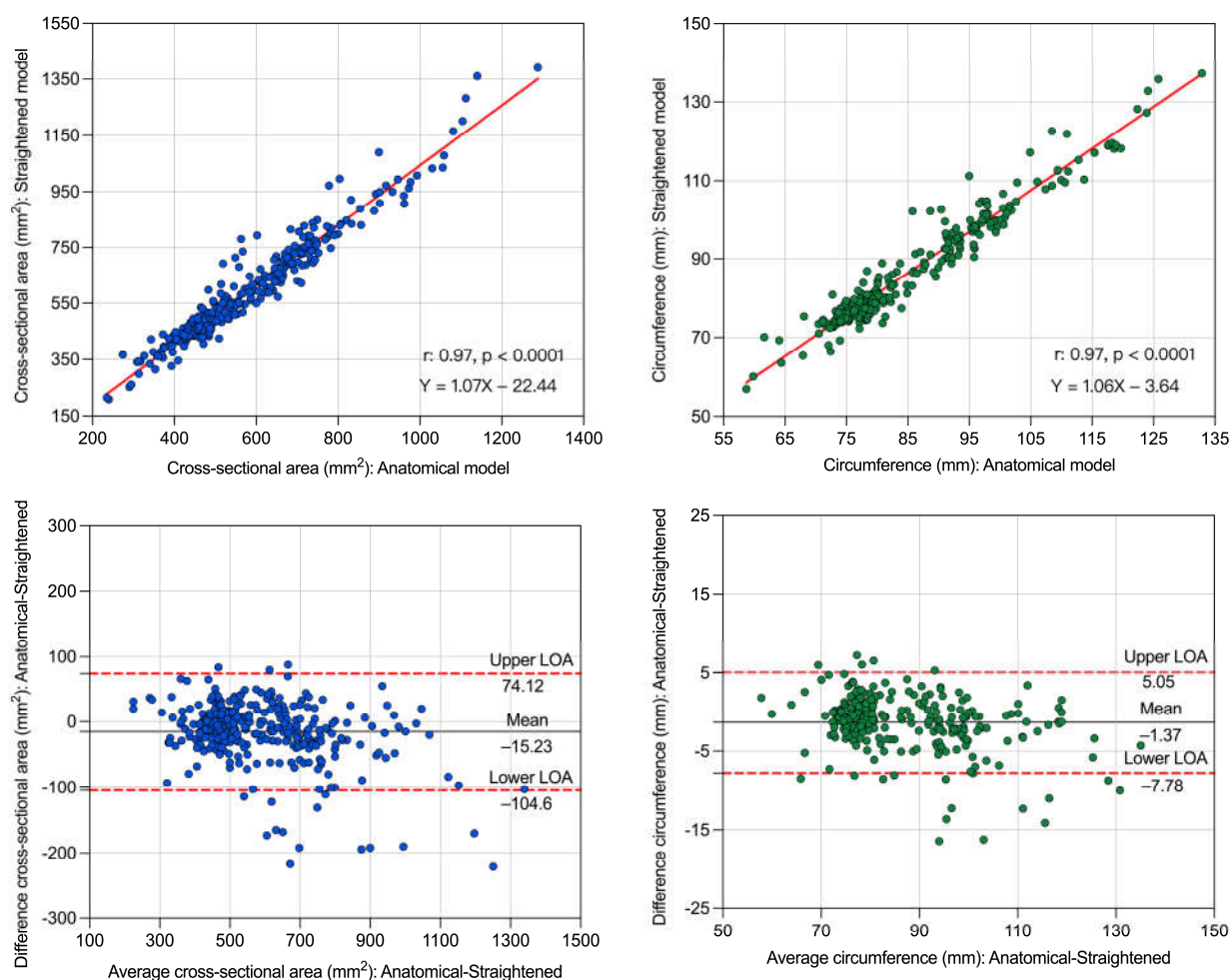
Figure 4. Pearson correlation scatterplot and Bland–Altman plot of cross-sectional area and circumference for the agreement between the anatomical model and straightened model from post-CT. LOA—limit of agreement.

The post-CT anatomical model and straightened model for the minimum diameter and maximum diameter were highly correlated, with a Pearson correlation coefficient of 0.96 ($p < 0.0001$) for the minimum diameter and 0.91 ($p < 0.0001$) for the maximum diameter. The limits of agreement between the anatomical model and the straightened model were in a good range (Figure 5).
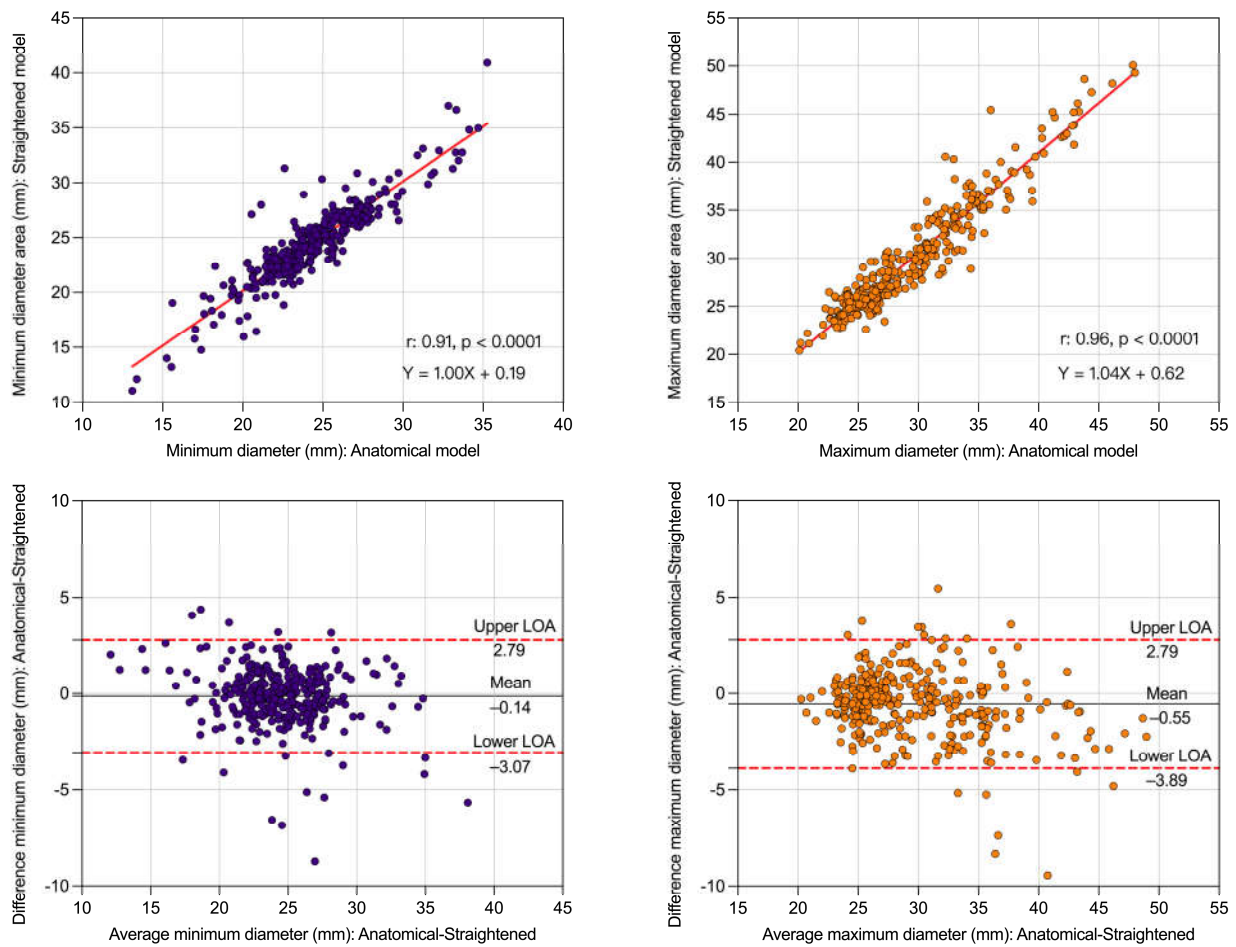
Figure 5. Pearson correlation scatterplot and Bland–Altman plot of minimum diameter and maximum diameter for the agreement between the anatomical model and straightened model from post-CT. LOA—limit of agreement.

The Pearson correlation coefficients and Bland–Altman agreements between the two model measurements of the annulus area, circumference, minimum diameter, and maximum diameter at each single plane are shown in Table 1. There was also an excellent correlation between every comparison. The results for the Pearson correlation coefficients and Bland–Altman analyses indicate a good accuracy of the straightened model.

Table 1. Pearson correlation coefficient and Bland–Altman analysis of cross-sectional area, circumference, minimum diameter, and maximum diameter for each single plane. CSA—cross-sectional area, C—circumference, LOA—limit of agreement, RVOT—right ventricular outflow tract, BPV—basal plane of pulmonary valve, STJ—sinotubular junction, PA—pulmonary artery, BPS—bottom plane of the stent, MPS—middle plane of the stent, TPS—top plane of the stent. * $p < 0.0001$.

Pre-CT		Pearson Correlation (r)	Bland–Altman Analysis		
			Mean Difference	Upper LOA	Lower LOA
RVOT	CSA (mm²)	0.96 *	−7.43	95.24	−110.10
	C (mm)	0.95 *	−0.23	10.05	−10.51
	Minimum diameter (mm)	0.94 *	−0.49	2.32	−3.31
	Maximum diameter (mm)	0.94 *	−0.54	4.05	−5.13
BPV	CSA (mm²)	0.87 *	−4.89	117.60	−127.40
	C (mm)	0.84 *	−0.89	12.23	−14.01

	Minimum diameter (mm)	0.88 *	−0.49	2.94	−3.92
	Maximum diameter (mm)	0.77 *	−0.18	6.03	−6.40
Sinus	CSA (mm²)	0.93 *	−5.00	54.53	−64.53
	C (mm)	0.94 *	−0.87	4.03	−5.76
	Minimum diameter (mm)	0.92 *	−0.34	1.29	−1.98
	Maximum diameter (mm)	0.90 *	−0.13	1.79	−2.04
STJ	CSA (mm²)	0.97 *	−14.30	30.54	−59.14
	C (mm)	0.97 *	−1.02	2.68	−4.72
	Minimum diameter (mm)	0.93 *	−0.61	1.15	−0.61
	Maximum diameter (mm)	0.94 *	−0.35	1.49	−2.18
PA	CSA (mm²)	0.97 *	−20.94	29.80	−71.68
	C (mm)	0.97 *	−1.67	2.24	−5.57
	Minimum diameter (mm)	0.95 *	−0.48	1.29	−2.25
	Maximum diameter (mm)	0.92 *	−0.73	1.71	−3.17
RVOT	CSA (mm²)	0.97 *	−37.39	110.10	−184.90
	C (mm)	0.97 *	−2.70	7.53	−12.92
	Minimum diameter (mm)	0.91 *	−0.40	4.94	−5.73
	Maximum diameter (mm)	0.93 *	−1.47	3.52	−6.46
BPS	CSA (mm²)	0.95 *	0.96	67.47	−65.55
	C (mm)	0.95 *	0.13	5.44	−5.17
	Minimum diameter (mm)	0.84 *	0.05	2.11	−2.00
	Maximum diameter (mm)	0.93 *	0.06	2.73	−2.61
MPS	CSA (mm²)	0.99 *	−10.36	23.76	−44.47
	C (mm)	0.99 *	−0.78	1.87	−3.43
	Minimum diameter (mm)	0.92 *	−0.19	1.29	−1.67
	Maximum diameter (mm)	0.96 *	−0.24	1.49	−1.96
TPS	CSA (mm²)	0.97 *	−21.57	42.77	−85.91
	C (mm)	0.97 *	−1.74	3.26	−6.75
	Minimum diameter (mm)	0.93 *	0.11	1.92	−1.70
	Maximum diameter (mm)	0.97 *	−0.9	1.67	−3.47
PA	CSA (mm²)	0.97 *	−7.77	66.30	−81.84
	C (mm)	0.97 *	−0.40	5.57	−6.38
	Minimum diameter (mm)	0.92 *	−0.27	1.85	−2.39
	Maximum diameter (mm)	0.94 *	−0.18	2.77	−3.13

3.3. Dynamic Variation of Landing Zone

The mean cross-sectional area and circumference dynamic variations of each plane during the whole cardiac cycle for the pre- and the post-CTs are shown in Figures 6 and 7. There was high variation in the RVOT and BPV cross-sectional area for the pre-CTs in the ten phases of the cardiac cycle, especially from 50% to 60% and 90% to 100%. For the straightened pre-CT model, the maximum and minimum mean annulus areas of the RVOT plane were 646 ± 149 mm² (90%) and 272 ± 122 mm² (50%), respectively, and the maximum and minimum cross-sectional area mean values of the BPV plane were 471 ± 48 mm² (100%) and 266 ± 101 mm² (60%), respectively. In addition, the post-CT RVOT annulus area differed greatly between 100% and 50% with areas of 1028 ± 210 mm² and 435 ± 144 mm², respectively. The dynamic variation trends for the circumference were similar to those for the cross-sectional area. The detailed mean differences (±standard deviation) of the cross-sectional area and the circumference are presented in Table S1. However, the variation in the BPS plane area in the post-CTs was small because the radial force of the implanted stent fixed the stent on the annulus between the BPS and the PA plane, allowing the PA to expand fully, which also led to an increase in the annulus ellipticity of the BPS plane (Table 2). The annulus of the RVOT plane has a more notable elliptical geometry

than the other planes. The detailed ellipticity indices of the five planes during the ten cardiac phases are presented in Table S2.
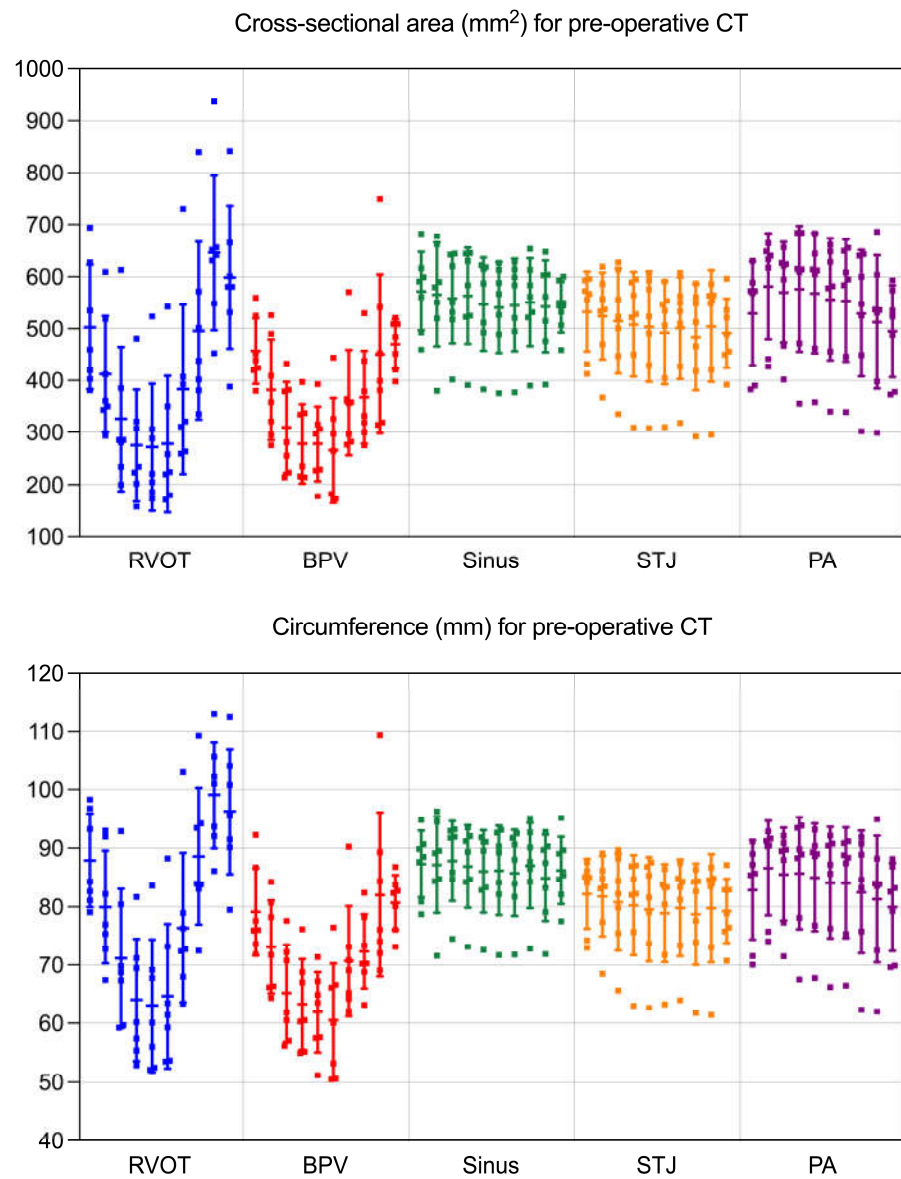
Cross-sectional area (mm^2) for pre-operative CT

Circumference (mm) for pre-operative CT

Figure 6. Dynamic variation in the cross-sectional area and circumference throughout the cardiac cycle at five planes from pre-operative CT. RVOT—right ventricular outflow tract, BPV—basal plane of pulmonary valve, STJ—sinotubular junction, PA—pulmonary artery. In each plane, one error bar indicates one frame (from 10% to 100%) in the cardiac cycle.
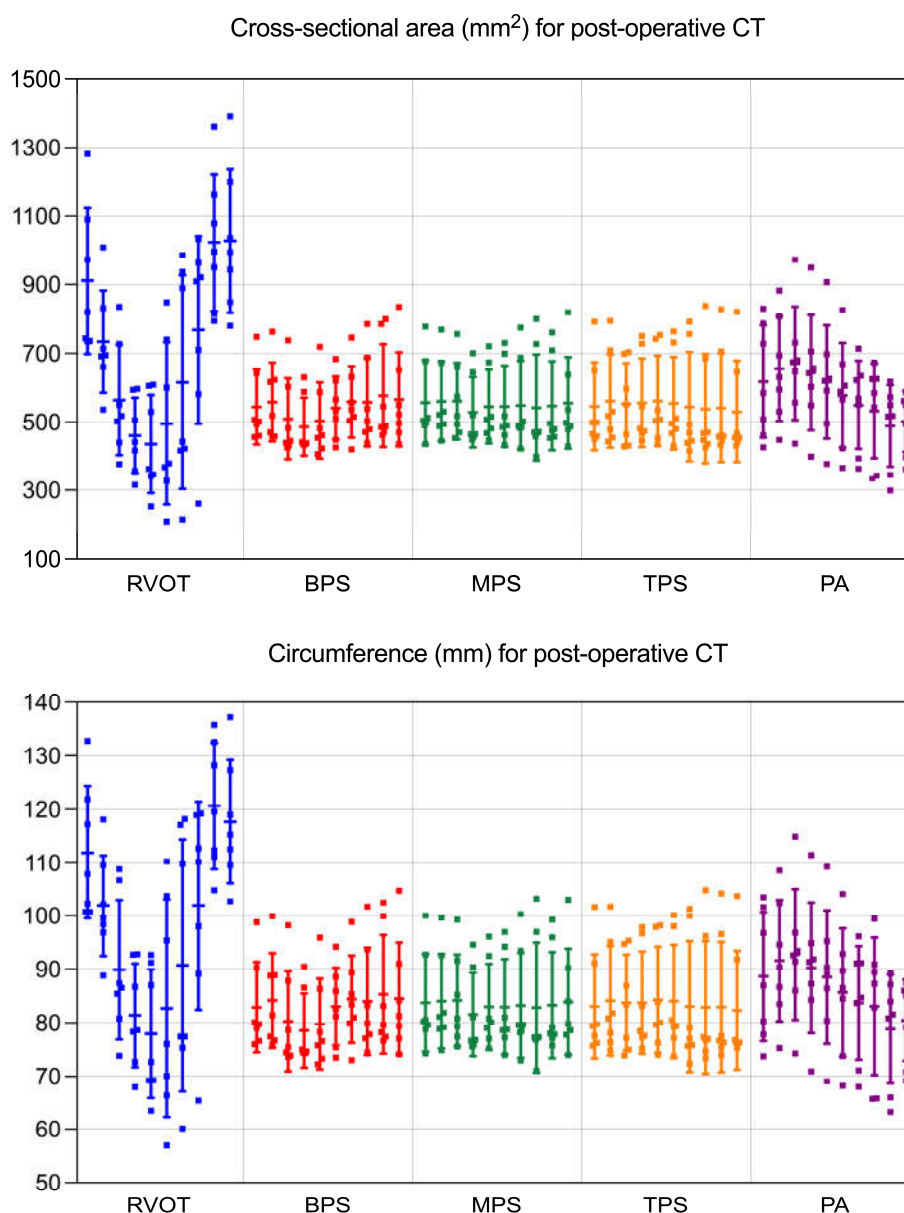
Cross-sectional area (mm^2) for post-operative CT

Circumference (mm) for post-operative CT

Figure 7. Dynamic variation in the cross-sectional area and circumference throughout the cardiac cycle at five planes from post-operative CT. RVOT—right ventricular outflow tract, BPS—bottom plane of the stent, MPS—middle plane of the stent, TPS—top plane of the stent, PA—pulmonary artery. In each plane, one error bar indicates one frame (from 10% to 100%) in the cardiac cycle.

Table 2. Annulus ellipticity index of five planes for pre-operative CT and post-operative CT. The ellipticity index was defined as minimum diameter/maximum diameter.

Ellipticity Index			
Pre-CT		**Post-CT**	
RVOT	0.55 ± 0.08	RVOT	0.69 ± 0.10
BPV	0.69 ± 0.12	BPS	0.88 ± 0.08
Sinus	0.89 ± 0.06	MPS	0.88 ± 0.09
STJ	0.90 ± 0.06	TPS	0.84 ± 0.10
PA	0.83 ± 0.06	PA	0.86 ± 0.09

4. Discussion

In this study, we illustrated the feasibility and accuracy of multiparametric analyses of the landing zone using 4D straightened segmentation generated from 4D C-CTA in sheep to measure and characterize the dynamic changes in the landing zone in pre-CTs and the implanted stent in post-CTs for TPVR at five selected planes. Furthermore, we used this methodology to obtain the 4D RV volume from all CTs, the landing zone volume from pre-CTs, the stent volume from post-CTs, and the ellipticity index at the selected planes, all of which could be used to estimate the right heart function, new heart valve selection, stent conditions following TPVR, and to help us gain a better understanding of the deformation of the landing zone at the native RVOT. Finally, we determined the differences in the cross-sectional area and perimeter on the selected pulmonary artery plane and the RVOT plane by comparing the corresponding pre- and post-CTs, thus reflecting the structural changes after TPVR. Compared with anatomical 4D segmentation, this straightened model not only has the comparable accuracy of relative measurement, but it also aids in better understanding the deformation of the landing zone at the native RVOT and the implanted stent, while supporting the development of new TPVR devices that are not only morphologically appropriate for the majority of patients scheduled to undergo TPVR, but also achieve better mechanical performance in the long term. Additionally, this straightened 4D segmentation aids in determining proper valve sizing by measuring the parameters in the appropriate planes.

Methods involving 3D echocardiography, fluoroscopy imaging, and 3D C-CTA are usually employed to evaluate cross-sectional changes at the RVOT, which are based on 3D alignment and fixed-plane segmentation [16–18]. Currently, 4D C-CTA can measure and characterize the changes in heart morphology and size throughout the cardiac cycle [19]. However, the current method for 4D segmentation is based on anatomical right heart reconstruction, which can neither fully describe the features of the RVOT-PA nor reveal intuitive observations. Furthermore, there is no method to quantify the RVOT-PA using comprehensive 4D C-CTA analysis. Along with the 4D anatomical segmentation, the angle between the RVOT and the main pulmonary artery may prevent the measuring lines from perfectly aligning with the planes of the landing zone (such as the annular plane and the sinotubular junction plane, which are extremely important for TPVR), which could lead to inaccurate landing zone measurements. Additionally, as the landing zone for TPVR is not a straight conduit, this could increase the difficulty of placing the planes in the right position, as well as the measurements. In clinical practice, it is crucial to obtain the precise length of the TPVR landing zone to avoid right and/or left pulmonary artery occlusion when adapting a self-expandable stented heart valve. In addition, in the landing zone for TPVR, only the RVOT plane and main pulmonary artery plane are the "real 2D flat planes." The other three planes, STJ, sinus, and the basal plane of the pulmonary valve, are defined by three points (STJ—the three commissures; sinus—the three peaks of the sinuses; and the basal plane of the pulmonary valve—the nadir of the pulmonary valve). These three planes are virtual planes, or at least not 2D flat planes; they are characterized by 3D features. Even multi-planar measurements are widely used in clinical practice to evaluate the RVOT prior to TPVR, but planes could be placed inaccurately in anatomical segmentations due to their 3D features and the angle of observation. In this study, we applied a 4D straightened segmentation with comparable accuracy and efficacy for five planar measurements from seven pre-CTs and seven post-CTs, which not only illustrates and visualizes the right heart's total deformation throughout the cardiac cycle but also quantitatively characterizes the RVOT as a whole. All measurements at the necessary planes can be easily checked using this 4D straightened segmentation. The cross-sectional area, circumference, and max–min diameters measured from the 4D straightened models show a strong linear correlation and strong agreement with the 4D anatomical models. With the 4D straightened models from the pre-CTs, the cross-sectional area and circumference were found to vary greatly at the RVOT and the BPV compared with the other three planes, which is consistent with anatomical measurements from a previous study

[12]; however, only the values at the RVOT were found to vary greatly from those derived from the post-CTs.

It is evident that single parameters alone are unable to reflect the features of the right heart clearly and comprehensively. Therefore, multiple parameters are needed to enable adequate pre- and post-TPVR evaluation of the right heart. Conventionally, cardiac function is assessed by 2D/3D echocardiography and cardiac magnetic resonance imaging (MRI) and is based mainly on the left ventricular ejection fraction (LVEF) and not the RVEF [20,21]. Furthermore, the RV volume cannot be evaluated precisely by echocardiography during clinical application due to the patient's complex anatomy after open-heart surgery and the influence of breathing. In order to address this issue and improve the evaluation, RV volume should be estimated by multiple parameters. In this context, 4D RV volume measurements from 4D C-CTA could play an important role. We successfully segmented and calculated 4D RV volume from pre- and post-CT (Table S1) to measure the distance between the right ventricular inflow tract and the RVOT, which allowed for the innovation of the delivery system and the planning of the access route for TPVR according to the length of the delivery system from pre-CT, evaluating the RVEF perioperatively. In addition, for the pre- and post-TPVR evaluation, we defined volume among the five dynamic planes as our specific landing zone for our self-designed TPVR device and quantitatively measured the volume deformation throughout the entire cardiac cycle to obtain directly perceived motions, such as the dynamics of the landing zone volume, the implanted stent volume, and the native PV volume (Table S1). Two of the enrolled sheep (sheep F and J) were selected for a representative illustration of the 4D dynamic segmentation (Videos S1–S8). Additionally, calculating the 4D ellipticity index of the implanted stent allowed us to easily observe the stent deformations during the cardiac cycle and evaluate the stented valve size.

The morphology of the implanted stent after full deployment is crucial for the new heart valve to function. Improper morphology of the implanted stent could give rise to a paravalvular leak or new heart valve regurgitation and could result in an inefficient opening area, which could lead to poor long-term performance [9,11,22]. In order to prevent the improper morphology of the implanted stent, a better understanding of the anatomy and device innovation are critical. We calculated the 4D ellipticity index of the landing zone from pre- and post-CT, which showed a lower ellipticity index at the RVOT and the BPV planes compared with the three other planes from pre-CT, while only the RVOT had a lower ellipticity index in post-CT because of the fixation of the implanted stent. The oval geometry of the BPV is an indicator of whether patients will benefit from TPVR because the myocardium at the BPV level would squeeze the stent into an undesirable geometry during the systolic phase, which could lead to an inefficient opening area in the new heart valve. The changes in the cross-sectional area and circumference during the cardiac cycle should also be taken into account for proper valve sizing, which is conventionally performed within 3D C-CTA by selecting the end-diastolic phase. However, based on the results of our study, it may be more expedient to select the mid-systolic phase for valve sizing because the largest cross-sectional area and circumference at the BPV and the STJ could prevent an elliptical geometry in the implanted stent. Additionally, a comprehensive evaluation of the "neighborhood" surrounding the left coronary artery is required. This could also encourage medical engineers to develop elliptical stents and heart valves with new features.

This study has several limitations. First, the accuracy and feasibility of the 4D straightened model were only demonstrated with seven pre-CTs and seven post-CTs, and need to be further proven with a larger population. Additionally, all pre-CTs were obtained from healthy sheep without any congenital heart defects. For clinical application, especially in patients who have undergone transannular patch repair/Ross procedures or other open-heart surgeries, additional work would be required to reconstruct the heart's architecture due to artifacts from adhesions between the pericardium and the myocardium, the stent, and the distorted anatomy. To our knowledge, two major artefacts that

significantly affect CT imaging accuracy are the blooming artefact and cardiac movement artefact [23,24]. With technical innovation, by reducing image noises and blooming artefacts, iterative reconstruction (IR) algorithms have the potential to enhance the quality of CT images. Compared to in vivo data, imaging data created from patient-specific models could provide accurate patient-specific geometry parameters without motion artefacts. However, in future studies, the acquisition times and contrast resolutions of scanners still need to be improved to obtain higher accuracy in CT imaging, which would improve the evaluation of TPVR outcomes.

5. Conclusions

Four-dimensional straightened segmentation can be a useful method for periprocedural evaluations for TPVR and could assist TPVR device innovation in the future.

6. Patents

There is no patent resulting from the work reported in this manuscript.

Supplementary Materials: The following supporting information can be downloaded at https://www.mdpi.com/article/10.3390/app122412912/s1, Table S1: The mean value of parameters for each plane during the cardiac cycle; Table S2: Ellipticity index for each plane during the cardiac cycle; Video S1: The deformation of 4D reconstructed anatomical segmentation from sheep F's pre-CT. Anterior view of the anatomical 4D segmentation with landing zone markers at the five selected planes, 1–6 s. Posterior view of the anatomical 4D segmentation with landing zone markers at the five selected planes, 6–13 s. Superior view of the anatomical 4D segmentation with landing zone markers at the five selected planes, 13–19 s; Video S2: The deformation of 4D reconstructed straightened segmentation from sheep F's pre-CT. Anterior view of the straightened 4D segmentation with landing zone markers at the five selected planes, 1–6 s. Posterior view of the straightened 4D segmentation with landing zone markers at the five selected planes, 6–13 s. Superior view of the straightened 4D segmentation with landing zone markers at the five selected planes, 13–19 s; Video S3: The deformation of 4D reconstructed anatomical segmentation from sheep F's post-CT. Anterior view of the anatomical 4D segmentation with landing zone markers at the five selected planes (with/without the implanted stent), 1–23 s. Posterior view of the anatomical 4D segmentation with landing zone markers at the five selected planes (with/without the implanted stent), 23–46 s. Superior view of the anatomical 4D segmentation with landing zone markers at the five selected planes (with/without the implanted stent), 46–69 s; Video S4: The deformation of 4D reconstructed straightened segmentation from sheep F's post-CT. Anterior view of the straightened 4D segmentation with landing zone markers at the five selected planes (with/without the implanted stent), 1–12 s. Posterior view of the straightened 4D segmentation with landing zone markers at the five selected planes (with/without the implanted stent), 12–24 s. Superior view of the straightened 4D segmentation with landing zone markers at the five selected planes (with/without the implanted stent), 24–37 s; Video S5: The deformation of 4D reconstructed anatomical segmentation from sheep J's pre-CT. Anterior view of the anatomical 4D segmentation with landing zone markers at the five selected planes, 1–6 s. Posterior view of the anatomical 4D segmentation with landing zone markers at the five selected planes, 6–13 s. Superior view of the anatomical 4D segmentation with landing zone markers at the five selected planes, 13–19 s; Video S6: The deformation of 4D reconstructed straightened segmentation from sheep J's pre-CT. Anterior view of the straightened 4D segmentation with landing zone markers at the five selected planes, 1–6 s. Posterior view of the straightened 4D segmentation with landing zone markers at the five selected planes, 6–13 s. Superior view of the straightened 4D segmentation with landing zone markers at the five selected planes, 13–20 s; Video S7: The deformation of 4D reconstructed anatomical segmentation from sheep J's post-CT. Anterior view of the anatomical 4D segmentation with landing zone markers at the five selected planes (with/without the implanted stent), 1–13 s. Posterior view of the anatomical 4D segmentation with landing zone markers at the five selected planes (with/without the implanted stent), 13–25 s. Superior view of the anatomical 4D segmentation with landing zone markers at the five selected planes (with/without the implanted stent), 25–38 s; Video S8: The deformation of 4D reconstructed straightened segmentation from sheep J's post-CT. Anterior view of the straightened 4D segmentation with landing zone markers at the five selected planes (with/without the implanted stent), 1–12 s. Posterior view of the straightened 4D segmentation with landing zone markers at the five selected planes (with/without

the implanted stent), 12–24 s. Superior view of the straightened 4D segmentation with landing zone markers at the five selected planes (with/without the implanted stent), 24–37 s.

Author Contributions: Conceptualization, X.S., Y.H. and B.S.; methodology, X.S., Y.H. and B.S.; validation, X.S., Y.H. and B.S.; formal analysis, Y.H. and B.S.; investigation, X.S., Y.H., M.S., A.B.-A., J.F.S.K., J.E., M.B.K., F.B. and B.S.; resources, X.S., Y.H., M.S., A.B.-A., J.F.S.K., J.E., M.B.K., F.B. and B.S.; data curation, Y.H.; writing—original draft preparation, X.S., Y.H. and B.S.; writing—review and editing, Y.H., F.B. and B.S.; visualization, X.S., Y.H., M.S., A.B.-A., J.F.S.K., J.E., M.B.K., F.B. and B.S.; supervision, B.S. and F.B.; project administration, X.S., Y.H. and B.S.; funding acquisition, B.S. All authors have read and agreed to the published version of the manuscript.

Institutional Review Board Statement: The animal study protocol, involving transcatheter pulmonary valve replacement from autologous pericardium with a self-expandable stent in a sheep model, was approved by the Ethics Committee of the Regional Office for Health and Social Affairs in Berlin (LaGeSo) (protocol code: IC14 g 0062/18, date of approval: 16 August 2018).

Informed Consent Statement: Not applicable.

Data Availability Statement: The data presented in this study are available in Supplementary Material.

Conflicts of Interest: The authors declare no conflicts of interest.

References

1. Bonhoeffer, P.; Boudjemline, Y.; Saliba, Z.; Merckx, J.; Aggoun, Y.; Bonnet, D.; Acar, P.; Le Bidois, J.; Sidi, D.; Kachaner, J. Percutaneous replacement of pulmonary valve in a right-ventricle to pulmonary-artery prosthetic conduit with valve dysfunction. *Lancet* **2000**, *356*, 1403–1405. https://doi.org/10.1016/s0140-6736(00)02844-0.
2. Georgiev, S.; Ewert, P.; Eicken, A.; Hager, A.; Hörer, J.; Cleuziou, J.; Meierhofer, C.; Tanase, D. Munich Comparative Study: Prospective Long-Term Outcome of the Transcatheter Melody Valve Versus Surgical Pulmonary Bioprosthesis With Up to 12 Years of Follow-Up. *Circ. Cardiovasc. Interv.* **2020**, *13*, e008963. https://doi.org/10.1161/circinterventions.119.008963.
3. McElhinney, D.B.; Zhang, Y.; Aboulhosn, J.A.; Morray, B.H.; Biernacka, E.K.; Qureshi, A.M.; Torres, A.J.; Shahanavaz, S.; Goldstein, B.H.; Cabalka, A.K.; et al. Multicenter Study of Endocarditis After Transcatheter Pulmonary Valve Replacement. *J. Am. Coll. Cardiol.* **2021**, *78*, 575–589. https://doi.org/10.1016/j.jacc.2021.05.044.
4. McElhinney, D.B.; Zhang, Y.; Levi, D.S.; Georgiev, S.; Biernacka, E.K.; Goldstein, B.H.; Shahanavaz, S.; Qureshi, A.M.; Cabalka, A.K.; Bauser-Heaton, H.; et al. Reintervention and Survival After Transcatheter Pulmonary Valve Replacement. *J. Am. Coll. Cardiol.* **2022**, *79*, 18–32. https://doi.org/10.1016/j.jacc.2021.10.031.
5. Chatterjee, A.; Bajaj, N.S.; McMahon, W.S.; Cribbs, M.G.; White, J.S.; Mukherjee, A.; Law, M.A. Transcatheter Pulmonary Valve Implantation: A Comprehensive Systematic Review and Meta-Analyses of Observational Studies. *J. Am. Heart Assoc.* **2017**, *6*, e006432. https://doi.org/10.1161/jaha.117.006432.
6. Rinaldi, E.; Sadeghi, S.; Rajpal, S.; Boe, B.A.; Daniels, C.; Cheatham, J.; Sinha, S.; Levi, D.S.; Aboulhosn, J. Utility of CT Angiography for the Prediction of Coronary Artery Compression in Patients Undergoing Transcatheter Pulmonary Valve Replacement. *World J. Pediatr. Congenit. Heart Surg.* **2020**, *11*, 295–303. https://doi.org/10.1177/2150135120905670.
7. Elattar, M.A.; Vink, L.W.; van Mourik, M.S.; Baan, J., Jr.; vanBavel, E.T.; Planken, R.N.; Marquering, H.A. Dynamics of the aortic annulus in 4D CT angiography for transcatheter aortic valve implantation patients. *PLoS ONE* **2017**, *12*, e0184133. https://doi.org/10.1371/journal.pone.0184133.
8. Ooms, J.F.; Wang, D.D.; Rajani, R.; Redwood, S.; Little, S.H.; Chuang, M.L.; Popma, J.J.; Dahle, G.; Pfeiffer, M.; Kanda, B.; et al. Computed Tomography-Derived 3D Modeling to Guide Sizing and Planning of Transcatheter Mitral Valve Interventions. *JACC Cardiovasc. Imaging* **2021**, *14*, 1644–1658. https://doi.org/10.1016/j.jcmg.2020.12.034.

9. Pluchinotta, F.R.; Sturla, F.; Caimi, A.; Giugno, L.; Chessa, M.; Giamberti, A.; Votta, E.; Redaelli, A.; Carminati, M. 3-Dimensional personalized planning for transcatheter pulmonary valve implantation in a dysfunctional right ventricular outflow tract. *Int. J. Cardiol.* **2020**, *309*, 33–39. https://doi.org/10.1016/j.ijcard.2019.12.006.

10. Chung, R.; Taylor, A.M. Imaging for preintervention planning: Transcatheter pulmonary valve therapy. *Circ. Cardiovasc. Imaging* **2014**, *7*, 182–189. https://doi.org/10.1161/circimaging.113.000826.

11. Curran, L.; Agrawal, H.; Kallianos, K.; Kheiwa, A.; Lin, S.; Ordovas, K.; Mahadevan, V.S. Computed tomography guided sizing for transcatheter pulmonary valve replacement. *Int. J. Cardiol. Heart Vasc.* **2020**, *29*, 100523. https://doi.org/10.1016/j.ijcha.2020.100523.

12. Schievano, S.; Capelli, C.; Young, C.; Lurz, P.; Nordmeyer, J.; Owens, C.; Bonhoeffer, P.; Taylor, A.M. Four-dimensional computed tomography: A method of assessing right ventricular outflow tract and pulmonary artery deformations throughout the cardiac cycle. *Eur. Radiol.* **2011**, *21*, 36–45. https://doi.org/10.1007/s00330-010-1913-5.

13. Gillespie, M.J.; Benson, L.N.; Bergersen, L.; Bacha, E.A.; Cheatham, S.L.; Crean, A.M.; Eicken, A.; Ewert, P.; Geva, T.; Hellenbrand, W.E.; et al. Patient Selection Process for the Harmony Transcatheter Pulmonary Valve Early Feasibility Study. *Am. J. Cardiol.* **2017**, *120*, 1387–1392. https://doi.org/10.1016/j.amjcard.2017.07.034.

14. Sun, X.; Hao, Y.; Sebastian Kiekenap, J.F.; Emeis, J.; Steitz, M.; Breitenstein-Attach, A.; Berger, F.; Schmitt, B. Four-Dimensional Computed Tomography-Guided Valve Sizing for Transcatheter Pulmonary Valve Replacement. *Thorac. Cardiovasc. Surg.* **2022**, *70*, S67–S103. https://doi.org/10.3791/63367.

15. Hao, Y.; Sun, X.; Kiekenap, J.F.S.; Emeis, J.; Steitz, M.; Breitenstein-Attach, A.; Berger, F.; Schmitt, B. Transcatheter Pulmonary Valve Replacement from Autologous Pericardium with a Self-Expandable Nitinol Stent in an Adult Sheep Model. *J. Vis. Exp.* **2022**. https://doi.org/10.3791/63661.

16. Kang, S.L.; Benson, L. Recent advances in cardiac catheterization for congenital heart disease. *F1000Res* **2018**, *7*, 370. https://doi.org/10.12688/f1000research.13021.1.

17. Kovács, A. 3D Echocardiography: Toward a Better Understanding of Cardiac Anatomy and Function. *J. Vis. Exp.* **2021**. https://doi.org/10.3791/63565.

18. Krishnaswamy, A.; Tuzcu, E.M.; Kapadia, S.R. Integration of MDCT and fluoroscopy using C-arm computed tomography to guide structural cardiac interventions in the cardiac catheterization laboratory. *Catheter. Cardiovasc. Interv.* **2015**, *85*, 139–147. https://doi.org/10.1002/ccd.25392.

19. Kidoh, M.; Utsunomiya, D.; Funama, Y.; Ashikaga, H.; Nakaura, T.; Oda, S.; Yuki, H.; Hirata, K.; Iyama, Y.; Nagayama, Y.; et al. Vectors through a cross-sectional image (VCI): A visualization method for four-dimensional motion analysis for cardiac computed tomography. *J. Cardiovasc. Comput. Tomogr.* **2017**, *11*, 468–473. https://doi.org/10.1016/j.jcct.2017.09.010.

20. Kucukseymen, S.; Arafati, A.; Al-Otaibi, T.; El-Rewaidy, H.; Fahmy, A.S.; Ngo, L.H.; Nezafat, R. Noncontrast Cardiac Magnetic Resonance Imaging Predictors of Heart Failure Hospitalization in Heart Failure With Preserved Ejection Fraction. *J. Magn. Reson. Imaging* **2022**, *55*, 1812–1825. https://doi.org/10.1002/jmri.27932.

21. Ostvik, A.; Salte, I.M.; Smistad, E.; Nguyen, T.M.; Melichova, D.; Brunvand, H.; Haugaa, K.; Edvardsen, T.; Grenne, B.; Lovstakken, L. Myocardial Function Imaging in Echocardiography Using Deep Learning. *IEEE Trans. Med. Imaging* **2021**, *40*, 1340–1351. https://doi.org/10.1109/tmi.2021.3054566.

22. Condado, J.F.; Corrigan, F.E., 3rd; Lerakis, S.; Parastatidis, I.; Stillman, A.E.; Binongo, J.N.; Stewart, J.; Mavromatis, K.; Devireddy, C.; Leshnower, B.; et al. Anatomical risk models for paravalvular leak and landing zone complications for balloon-expandable transcatheter aortic valve replacement. *Catheter. Cardiovasc. Interv.* **2017**, *90*, 690–700. https://doi.org/10.1002/ccd.26987.

23. De Ponti, E.; Morzenti, S.; Crivellaro, C.; Elisei, F.; Crespi, A.; Guerra, L. Motion Management in PET/CT: Technological Solutions. *Curr. Radiopharm.* **2018**, *11*, 79–85. https://doi.org/10.2174/1874471011666180419150440.

24. Liu, H.; Wingert, A.; Wang, J.; Zhang, J.; Wang, X.; Sun, J.; Chen, F.; Khalid, S.G.; Jiang, J.; Zheng, D. Extraction of Coronary Atherosclerotic Plaques From Computed Tomography Imaging: A Review of Recent Methods. *Front. Cardiovasc. Med.* **2021**, *8*, 597568. https://doi.org/10.3389/fcvm.2021.597568.